

A simple parametric model for spherical galaxy clusters

Malak Olamaie,^{1*} Michael P. Hobson¹ and Keith J. B. Grainge^{1,2}

¹ *Astrophysics Group, Cavendish Laboratory, 19 J. J. Thomson Avenue, Cambridge, CB3 0HE*

² *Kavli Institute for Cosmology Cambridge, Madingley Road, Cambridge, CB3 0HA*

Accepted 2012 March 21. Received 2012 March 2; in original form 2011 September 13

ABSTRACT

We present an analytic parametric model to describe the baryonic and dark matter distributions in clusters of galaxies with spherical symmetry. It is assumed that the dark matter density follows a Navarro, Frenk and White (NFW) profile and that the gas pressure is described by a generalised NFW (GNFW) profile. By further demanding hydrostatic equilibrium and that the local gas fraction is small throughout the cluster, one obtains unique functional forms, dependent on basic cluster parameters, for the radial profiles of all the properties of interest in the cluster. We show these profiles are consistent both with numerical simulations and multi-wavelength observations of clusters. We also use our model to analyse six simulated SZ clusters as well as A611 SZ data from the Arcminute Microkelvin Imager (AMI). In each case, we derive the radial profile of the enclosed total mass and the gas pressure and show that the results are in good agreement with our model prediction.

Key words: methods: data analysis – cosmology: observations – galaxies: clusters: general

1 INTRODUCTION

Analyses of observations of galaxy clusters via their X-ray emission, gravitational lensing or Sunyaev-Zel’dovich (SZ) effect are often based on some parameterised cluster model for the distribution of the cluster dark matter and the thermodynamical properties of its intra-cluster medium (ICM). The accuracy and robustness of cluster parameters derived from studies at different wavelengths depend greatly on how well the model describes the physical properties of the cluster, and the assumptions made regarding the dynamical state of the cluster and its gas content.

Cluster models typically assume spherical symmetry, an ideal gas equation-of-state, and parameterised functional forms for the radial distribution of two linearly-independent cluster properties, such as electron density and temperature (Sanderson & Ponman 2003; Vikhlinin et al. 2005, 2006; Laroque et al. 2006; Feroz et al. 2009; AMI Consortium: Zwart et al. 2011; AMI Consortium: Rodríguez-González et al. 2011; AMI Consortium: Hurley-Walker et al. 2012 and AMI Consortium: Shimwell et al. 2011); electron pressure and density (Nagai et al. 2007; Mroczkowski et al. 2009; Arnaud et al. 2010; Plagge et al. 2010 and Planck Collaboration 2011d); or electron pressure and entropy (Allison et al. 2011; AMI Consortium: Olamaie et al. 2012). Such parameterisations are usually supplemented by the imposition of a condition on the dynamical state of the cluster, most commonly hydrostatic equilibrium or a virial relation, together sometimes with further constraints, such as a constant gas fraction throughout the cluster and/or assorted scaling relations. All such models, with their corresponding assumptions, have the potential to introduce biases in

the derived cluster physical parameters, depending strongly on the appropriateness of the assumptions made and whether or not the data can constrain the parameters describing the model (see AMI Consortium: Olamaie et al. 2012).

A recent interesting example of a parameterised spherical cluster model by Mroczkowski (2011) assumes the cluster dark matter density to follow a parameterised Navarro, Frenk and White (NFW) (Navarro et al. 1997) profile and the gas pressure to be described by a generalised NFW (GNFW) profile (Nagai et al. 2007) with fixed shape parameters, both in accordance with numerical simulations. This model also assumes hydrostatic equilibrium and, crucially, a constant gas fraction (both local and enclosed) throughout the cluster, which is a very stringent condition. In this paper, we adapt this model by replacing this last condition, which is in fact inconsistent with the rest of the model, by the much weaker assumption that the local gas fraction throughout the cluster is small compared with unity. We show that this assumption leads to a unique solution for the radial dependence of all the cluster properties of interest (dependent on basic cluster parameters).

Further, we analyse six simulated clusters and one real cluster (A611) in this frame work through their Sunyaev–Zel’dovich effect and show that the resulting profiles agree with those predicted by numerical simulations and measured in multi-wavelength observations of galaxy clusters.

2 THE MODEL

The first assumption in our model is a functional form for the dark matter density $\rho_{\text{DM}}(r)$. Cosmological N -body simulations suggest that all dark matter halos can be modelled with the spherically aver-

* Email: mo323@mrao.cam.ac.uk

aged density profile of Navarro, Frenk and White (NFW) (Navarro et al. 1997)

$$\rho_{\text{DM}}(r) = \frac{\rho_s}{\left(\frac{r}{R_s}\right)\left(1 + \frac{r}{R_s}\right)^2}, \quad (1)$$

where ρ_s is an overall normalisation coefficient and R_s is the scale radius where the logarithmic slope of the profile $d \ln \rho(r)/d \ln r = -2$. It is common practice also to define the halo concentration parameter, $c_{200} = \frac{r_{200}}{R_s}$, where r_{200} is the radius at which the enclosed mean density is 200 times the critical density at the cluster redshift.

Our second assumption is a functional form for the gas pressure $P_{\text{gas}}(r)$. Numerical simulations (Nagai et al. 2007) and X-ray observations of clusters of galaxies using *Chandra* (Vikhlinin et al. 2005, 2006; Nagai 2006; Nagai et al. 2007) both show that self-similarity is more likely to be observed in the gas pressure profile than the density or temperature at large radii, i.e. up to r_{500} and beyond. The gas pressure is also the quantity least affected by dynamical history and non-gravitational mechanisms inside the ICM. In particular, following Nagai et al. (2007), we assume the electron pressure follows the GNFW profile

$$P_e(r) = \frac{P_{\text{ei}}}{\left(\frac{r}{r_p}\right)^c \left(1 + \left(\frac{r}{r_p}\right)^a\right)^{(b-c)/a}}, \quad (2)$$

where P_{ei} is an overall normalisation coefficient, r_p is the scale radius. It is common to define the latter in terms of r_{500} , the radius at which the mean enclosed density is 500 times the critical density at the cluster redshift, and the gas concentration parameter, $c_{500} = r_{500}/r_p$. The parameters (a, b, c) describe the slopes of the pressure profile at $r \approx r_p$, $r > r_p$ and $r \ll r_p$ respectively. In the simplest case, we follow Arnaud et al. (2010) and fix the values of the gas concentration parameter and the slopes to be $(c_{500}, a, b, c) = (1.156, 1.0620, 5.4807, 0.3292)$. Arnaud et al. (2010) derived these values by analysing profiles of the REXCESS cluster sample observed with XMM-Newton (Böhringer et al. 2007) as well as three different sets of detailed numerical simulations by Borgani et al. (2004), Piffaretti & Valdarini (2008) and Nagai et al. (2007) that take into account radiative cooling, star formation, and energy feedback from supernova explosions. They estimated M_{500} for each cluster in their sample using the standard $M_{500} - Y_x$ scaling relation (see Appendix B in Arnaud et al. 2010). It should be noted that these values are different from those used by Nagai et al. (2007), Mroczkowski et al. (2009), Plagge et al. (2010) and Mroczkowski (2011). The Arnaud values were, however, used to analyse SZ data from the Planck survey data (Planck Collaboration 2011d).

More generally, one can allow the parameters (c_{500}, a, b, c) to vary, although we will not consider this case here. Given the electron pressure, the gas pressure is then defined by

$$P_{\text{gas}}(r) = \frac{\mu_e}{\mu} P_e(r), \quad (3)$$

where $\mu_e = 1.14 m_p$ (Mason & Myers 2000) is the mean gas mass per electron, $\mu = 0.6 m_p$ is the mean mass per gas particle and m_p is the proton mass.

Our third assumption concerns the dynamical state of the cluster, which we take to be in hydrostatic equilibrium throughout. Thus, the total cluster mass internal to radius r is related to the gas pressure gradient at that radius by

$$\frac{dP_{\text{gas}}(r)}{dr} = -\rho_{\text{gas}}(r) \frac{GM_{\text{tot}}(r)}{r^2}. \quad (4)$$

However, we note that the latest cosmological simulations of galaxy clusters with focus on studying the cluster outskirts (Lau

et al. 2009; Battaglia et al. 2010; Nagai 2011; Nagai & Lau 2011; Parrish et al. 2012 and Battaglia et al. 2011 a,b) and observational studies of the clusters using the *Suzaku* and XMM-Newton satellites at large radii- out to the virial radius including A1795 (Bautz et al. 2009), PKS 0745-191 (George et al. 2009), A2204 (Reiprich et al. 2009), A1413 (Hoshino et al. 2010), A1689 (Kawaharada et al. 2010), Virgo cluster (Urban et al. 2011) and Perseus cluster (Simionescu et al. 2011), show that the presence of random gas motion, gas clumping and turbulence due to the magnothermal instability in the intracluster medium of galaxy clusters provide non-thermal pressure support and can introduce biases in HSE measurements of the ICM profiles and cluster mass. Hence in order to recover these profiles accurately we need to modify the equation of HSE to take into account non-thermal pressure components. However, as the studies of this kind (to understand the physics of the cluster outskirts and make accurate measurements of the ICM profiles in the cluster outer regions) are still ongoing, we do not study a modified form of HSE here. We, of course, aim to consider a more general form in our future analyses.

Finally, our model is completed by assuming that the local gas fraction is much less than unity throughout the cluster, i.e. $\frac{\rho_{\text{gas}}(r)}{\rho_{\text{tot}}(r)} \ll 1$ for all r . This final assumption allows us to write $\rho_{\text{tot}}(r) = \rho_{\text{DM}}(r) + \rho_{\text{gas}}(r) \approx \rho_{\text{DM}}(r)$. We emphasize that this assumption is for the gravitational part of the calculation and as we show in equation (6) we do not assume $\rho_{\text{gas}}(r) = 0$. Thus, from (1), the total mass enclosed with a radius r has the analytical solution

$$\begin{aligned} M_{\text{tot}}(r) &= \int_0^r \rho_{\text{DM}}(r') (4\pi r'^2 dr') \\ &= 4\pi \rho_s R_s^3 \left\{ \ln \left(1 + \frac{r}{R_s} \right) - \left(1 + \frac{R_s}{r} \right)^{-1} \right\}. \end{aligned} \quad (5)$$

Substituting this form and the expressions (2) and (3) for the gas pressure into the condition (4) for hydrostatic equilibrium, one may derive the gas density profile

$$\begin{aligned} \rho_{\text{gas}}(r) &= \left(\frac{\mu_e}{\mu} \right) \left(\frac{1}{4\pi G} \right) \left(\frac{P_{\text{ei}}}{\rho_s} \right) \left(\frac{1}{R_s^3} \right) \times \\ &\quad \frac{r}{\ln \left(1 + \frac{r}{R_s} \right) - \left(1 + \frac{R_s}{r} \right)^{-1}} \times \\ &\quad \left(\frac{r}{r_p} \right)^{-c} \left[1 + \left(\frac{r}{r_p} \right)^a \right]^{-\left(\frac{a+b-c}{a} \right)} \left[b \left(\frac{r}{r_p} \right)^a + c \right] \end{aligned} \quad (6)$$

The radial profile of the electron number density is then trivially obtained using $n_e(r) = \rho_{\text{gas}}(r)/\mu_e$. Assuming an ideal gas equation of state, this in turn yields the electron temperature profile $k_B T_e(r) = P_e(r)/n_e(r)$, given by

$$\begin{aligned} k_B T_e(r) &= (4\pi G \rho_s) (R_s^3) \times \\ &\quad \left[\frac{\ln \left(1 + \frac{r}{R_s} \right) - \left(1 + \frac{R_s}{r} \right)^{-1}}{r} \right] \times \\ &\quad \left[1 + \left(\frac{r}{r_p} \right)^a \right] \left[b \left(\frac{r}{r_p} \right)^a + c \right]^{-1} \end{aligned} \quad (7)$$

which is also equal to the gas temperature profile $k_B T_{\text{gas}}(r)$. We can also determine the radial profile for electron entropy of the ICM. In the astronomy literature, for an adiabatic monatomic gas, entropy is defined as $K_e = k_B T_e(r) n_e^{-2/3}(r)$ which is related to the true thermodynamic entropy per gas particle via $S = \frac{3}{2} k_B \ln(K_e) + S_0$ where S_0 is a constant (Voit 2005).

The only fundamental cluster property for which the radial profile cannot be expressed in an explicit analytical form is the gas mass enclosed within radius r ,

$$M_{\text{gas}}(r) = \int_0^r \rho_{\text{gas}}(r') (4\pi r'^2 dr'). \quad (8)$$

For the gas density profile in (6), we have been unable to evaluate this expression analytically, and so $M_{\text{gas}}(r)$ must be obtained using numerical integration. Consequently, the enclosed gas mass fraction profile $f_{\text{gas}}(r) = M_{\text{gas}}(r)/M_{\text{tot}}(r)$ also cannot be written in closed form. It is clear, however, that the resulting $f_{\text{gas}}(r)$ will not be constant. Therefore, this contradicts the assumption of Mroczkowski (2011) of $f_{\text{gas}}(r)$ being constant. In the next section, we represent the profile of $f_{\text{gas}}(r)$ which illustrates this point.

3 ILLUSTRATION OF CLUSTER PROPERTIES

In the simplest case, where a , b , c and c_{500} in (2) have fixed values, our cluster model depends only on three parameters: ρ_s and R_s in the NFW dark matter density profile (1) and P_{ei} in the pressure profile (2). One is, however, free to choose alternative parameters to define a cluster, although this choice and the priors imposed on the parameters can lead to very different results in the analysis of cluster observations (AMI Consortium: Olamaie et al. 2012). Here we will define clusters in terms of the parameter set $M_{\text{tot}}(r_{200})$, c_{200} , $f_{\text{gas}}(r_{200})$ and the redshift z , and investigate the resulting radial profiles of quantities of interest in our cluster model.

For illustration purposes, we will consider clusters at a fixed redshift $z = 0.3$. We will further assume that $f_{\text{gas}}(r_{200}) = 0.12$, which is reasonable since we expect the gas mass fraction to approach the universal baryon fraction at large scales near the virial radius (Komatsu et al. 2011; Larson et al. 2011). We will consider a selection of 15 clusters equally spaced in the mass range $1.0 \times 10^{14} M_{\odot} < M_{\text{tot}}(r_{200}) < 1.5 \times 10^{15} M_{\odot}$. For each cluster, we also consider 15 values of c_{200} in the range 4–6, since the concentration parameter shows a clear dependence on the halo mass, with massive halos having lower concentration parameter (Pointecouteau et al. 2005; Salvador-Solé et al. 2007; Vikhlinin et al. 2006). Throughout, we also assume a Λ CDM cosmology with $\Omega_M = 0.3$, $\Omega_{\Lambda} = 0.7$, $\sigma_8 = 0.8$, $h = 0.7$, $w_0 = -1$, $w_a = 0$.

To determine the radial profiles of quantities of interest for a given cluster, one must first determine the values of the model parameters ρ_s , R_s , r_p and P_{ei} . Since $M_{\text{tot}}(r_{200})$ is the total amount of matter internal to radius r_{200} , one may write

$$M_{\text{tot}}(r_{200}) = \frac{4\pi}{3} r_{200}^3 (200\rho_{\text{crit}}(z)). \quad (9)$$

Thus, for a given $M_{\text{tot}}(r_{200})$ and z , one may calculate r_{200} , and hence $R_s = r_{200}/c_{200}$. The value of ρ_s is then obtained by equating the input value of $M_{\text{tot}}(r_{200})$ with the RHS of (5) evaluated at $r = r_{200}$, and is given by

$$\rho_s = \frac{200}{3} \left(\frac{r_{200}}{R_s} \right)^3 \frac{\rho_{\text{crit}}(z)}{\left\{ \ln \left(1 + \frac{r_{200}}{R_s} \right) - \left(1 + \frac{R_s}{r_{200}} \right)^{-1} \right\}}. \quad (10)$$

By equating equations (5) and (9) at r_{500} , one may calculate r_{500} and hence $r_p = r_{500}/c_{500}$. Finally, P_{ei} is obtained by substituting (6) into (8), evaluating the RHS at $r = r_{200}$ and equating the result to $f_{\text{gas}}(r_{200})M_{\text{tot}}(r_{200})$. This yields

$$P_{\text{ei}} = \left(\frac{\mu}{\mu_e} \right) (G\rho_s R_s^3) M_{\text{gas}}(r_{200}) \times$$

Table 1. The input parameters and ranges used in the analysis

Parameter	Value
$M_{\text{tot}}(r_{200})$	$(1.0 \text{ } 15.0) \times 10^{14} M_{\odot}$
c_{200}	$(4 \text{ } 6)$
z	0.3
$f_{\text{g}}(r_{200})$	0.12

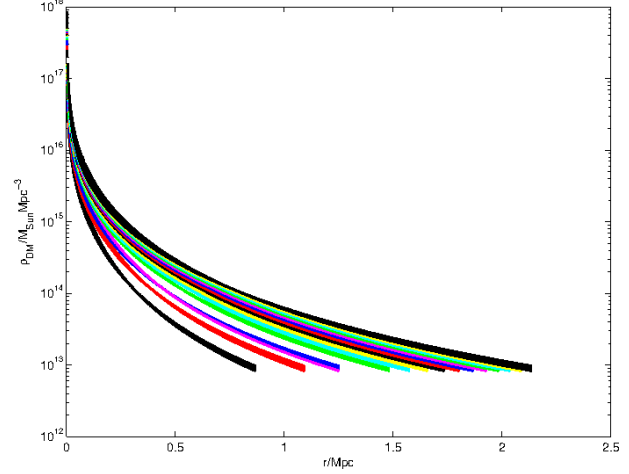


Figure 1. Dark matter density profiles $\rho_{\text{DM}}(r)$. For a given thick line, the thickness represents the spread in varying the halo concentration parameter, c_{200} between 4 and 6.

$$\frac{1}{\int_0^{r_{200}} r'^3 dr' \frac{\left[b \left(\frac{r'}{r_p} \right)^a + c \right]}{\left[\ln \left(1 + \frac{r'}{R_s} \right) - \left(1 + \frac{R_s}{r'} \right)^{-1} \right] \left(\frac{r'}{r_p} \right)^c \left[1 + \left(\frac{r'}{r_p} \right)^a \right]^{\left(\frac{a+b}{a-c} \right)}}, \quad (11)$$

which must be evaluated numerically.

Tab. 1 summarises the input parameter values for our illustrative clusters. The corresponding radial profiles for various quantities of interest are shown in Figs. 1–8. The thickness of each line represents the spread in halo concentration parameter corresponding to varying c_{200} between 4 and 6-i.e. each thick line represents clusters with the same $M_{\text{tot}}(r_{200})$ but different c_{200} . It should be noted that each profile is plotted out to r_{200} for the corresponding cluster.

4 ANALYSIS OF INTERFEROMETRIC SZ OBSERVATIONS

In order to verify that our proposed model, with its corresponding assumptions, can describe profiles of cluster physical properties accurately, we carried out a Bayesian analysis (Feroz & Hobson 2008; Feroz et al. 2009a) of a set of six simulated clusters as well as A611 observed through their Sunyaev-Zel'dovich (SZ) effect (Sunyaev & Zeldovich 1970; Birkinshaw 1999; Carlstrom, Holder & Reese 2002) using the Arcminute Microkelvin Imager (AMI) (AMI Consortium: Zwart et al. 2008).

The observed SZ surface brightness in the direction of electron reservoir may be described as

$$\delta I_{\nu} = T_{\text{CMB}} y f(\nu) \frac{\partial B_{\nu}}{\partial T} \bigg|_{T=T_{\text{CMB}}}. \quad (12)$$

Here B_{ν} is the blackbody spectrum, $T_{\text{CMB}} = 2.73$ K (Fixsen

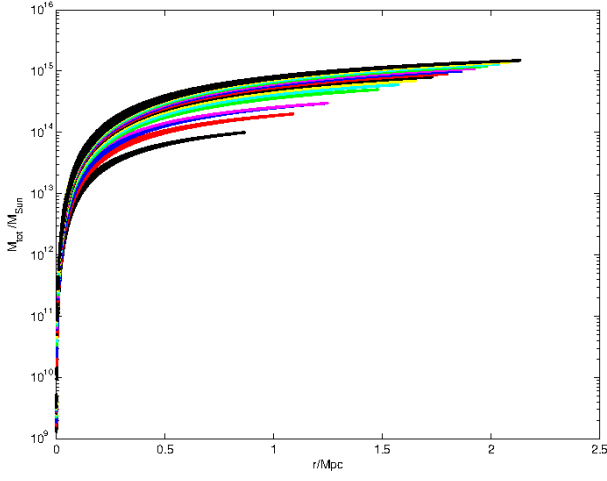


Figure 2. Integrated total mass profiles $M_{\text{tot}}(r)$.

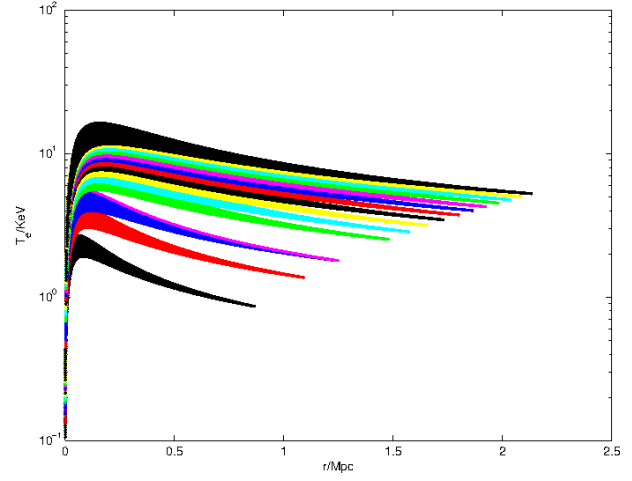


Figure 5. Electron temperature profiles $T_e(r)$.

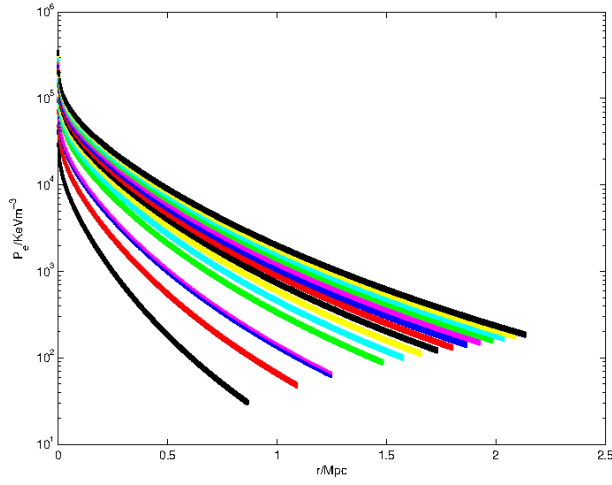


Figure 3. Electron pressure profiles $P_e(r)$.

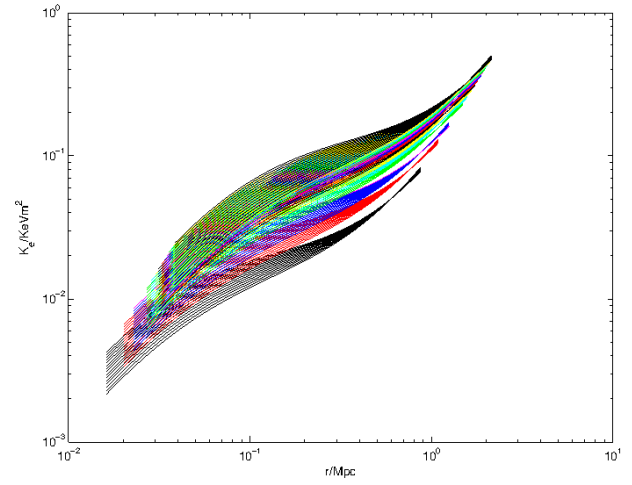


Figure 6. Electron entropy profiles $K_e(r)$.

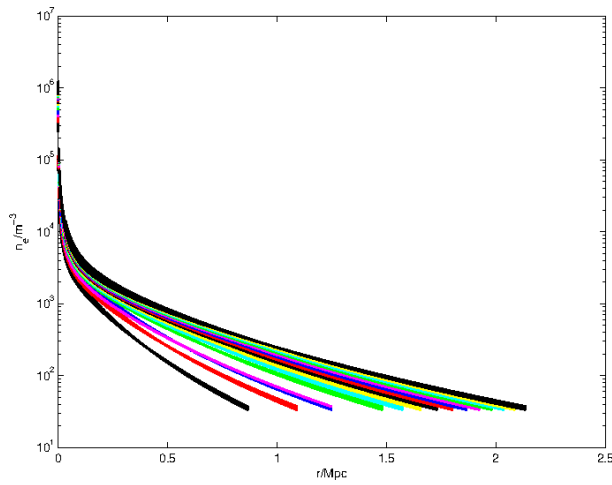


Figure 4. Electron number density profiles $n_e(r)$.

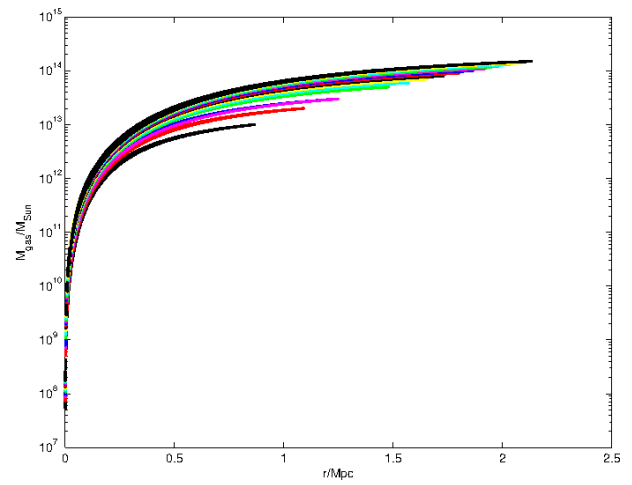


Figure 7. Gas mass profiles $M_{\text{gas}}(r)$.

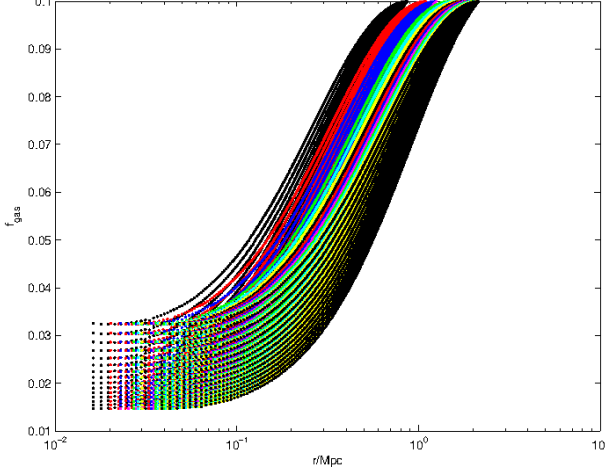


Figure 8. Gas mass fraction profiles $f_{\text{gas}}(r)$.

et al. 1996) is the temperature of the CMB radiation, $f(\nu) = (x \frac{e^x + 1}{e^x - 1} - 4)(1 + \delta(x, T_e))$ is the frequency dependence of thermal SZ signal, $x = \frac{h_p \nu}{k_B T_{\text{CMB}}}$, h_p is Planck's constant, ν is the frequency and k_B is Boltzmann's constant. $\delta(x, T_e)$ takes into account the relativistic corrections in the study of the thermal SZ effect which is due to the presence of thermal weakly relativistic electrons in the ICM and is derived by solving the Kompaneets equation up to the higher orders (Rephaeli 1995, Itoh et al. 1998, Nozawa et al. 1998, Pointecouteau et al. 1998 and Challinor and Lasenby 1998). It should be noted that at 15 GHz (AMI observing frequency) $x = 0.3$ and therefore the relativistic correction, as shown by Rephaeli (1995), is negligible for $k_B T_e \leq 15$ keV. The dimensionless parameter y , known as the Comptonization parameter, is the integral of the number of collisions multiplied by the mean fractional energy change of photons per collision, along the line of sight

$$y = \frac{\sigma_T}{m_e c^2} \int_{-\infty}^{+\infty} n_e(r) k_B T_e(r) dl \quad (13)$$

$$= \frac{\sigma_T}{m_e c^2} \int_{-\infty}^{+\infty} P_e(r) dl, \quad (14)$$

where $n_e(r)$, $P_e(r)$ and T_e are the electron number density, pressure and temperature at radius r respectively. σ_T is Thomson scattering cross-section, m_e is the electron mass, c is the speed of light and dl is the line element along the line of sight. It should be noted that in equation (13) we have used the ideal gas equation of state.

An interferometer like AMI operating at a frequency ν measures samples from the complex visibility plane $\tilde{I}_\nu(\mathbf{u})$. These are given by a weighted Fourier transform of the surface brightness $I_\nu(\mathbf{x})$, namely

$$\tilde{I}_\nu(\mathbf{u}) = \int A_\nu(\mathbf{x}) I_\nu(\mathbf{x}) \exp(2\pi i \mathbf{u} \cdot \mathbf{x}) d\mathbf{x}, \quad (15)$$

where \mathbf{x} is the position relative to the phase centre, $A_\nu(\mathbf{x})$ is the (power) primary beam of the antennas at observing frequency ν (normalised to unity at its peak) and \mathbf{u} is the baseline vector in units of wavelength.

Further details of our Bayesian methodology, modelling interferometric SZ data, primordial CMB anisotropies, and resolved and unresolved radio point-source models are given in Hobson & Maisinger (2002), Feroz & Hobson (2008) and (2009 a,b), AMI Consortium: Davies et al. (2011) and AMI Consortium: Olamaie et al. (2012).

Table 2. The input parameters used to generate simulated clusters.

Cluster	$M_{\text{tot}}(r_{200}) 10^{14} M_\odot$	c_{200}	z	$f_g(r_{200})$
clsim1	5.0	4.0	0.3	0.12
clsim2	5.0	4.3	0.3	0.12
clsim3	5.0	4.5	0.3	0.12
clsim4	5.0	5.0	0.3	0.12
clsim5	5.0	5.5	0.3	0.12
clsim6	5.0	6.0	0.3	0.12

In generating simulated SZ skies and observing them with a model AMI SA, we have used the methods outlined in Hobson & Maisinger (2002), Grainge et al. (2002), Feroz et al. (2009b) and AMI Consortium: Olamaie et al. (2012).

Generating a simulated cluster SZ signal using the model described in Sections 2 and 3 requires the input parameters $M_{\text{tot}}(r_{200})$, c_{200} , z and $f_{\text{gas}}(r_{200})$ listed in Tab. 1; this set of parameters fully describes the Comptonization y parameter. Tab. 2 summarises the input parameters used to generate six simulated SZ clusters. The simulated clusters all have the same $M_{\text{tot}}(r_{200})$, z and $f_{\text{gas}}(r_{200})$ and the only parameter that varies from cluster to cluster is the halo concentration parameter, c_{200} .

A611 is a rich cluster at redshift $z = 0.288$ and has been studied through its X-ray emission, strong lensing, weak lensing and SZ effect (Schmidt & Allen 2007; Romano et al. 2010; Donnarumma et al. 2011 and AMI Consortium: Shimwell et al. 2011). These studies suggest that there is no significant contamination from radio sources and there is no evidence for a radio halo associated with A611 (Venturi et al. 2008). The SZ signal (decrement) on the AMI map appears circular, (fig. 2 in AMI Consortium: Shimwell et al. 2011) in agreement with the X-ray surface brightness from the *Chandra* archive data (fig. 2 in AMI Consortium: Shimwell et al. 2011 and fig. 1 in Donnarumma et al. 2011), which also appears to be smooth and whose peak coincides with the position of the brightest cluster galaxy and the SZ peak. These results are a strong indication that the cluster is relaxed. Moreover, the absence of radio halos in the cluster which are major sources of the presence of non-thermal mechanisms in the galaxy clusters (Brunetti et al. 2009) makes A611 an ideal cluster candidate for our analysis as it satisfies both assumptions of spherical symmetry and thermal pressure support in equation of the HSE.

Details of AMI pointed observation towards the cluster, data reduction pipeline and mapping are described in AMI Consortium: Shimwell et al. (2011) and in here we focus on the Bayesian analysis of the clusters using our model.

The sampling parameters in our Bayesian analysis are $\Theta_c \equiv (x_c, y_c, c_{200}, M_{\text{tot}}(r_{200}), f_g(r_{200}), z)$, where x_c and y_c are cluster projected position on the sky. We further assume that the priors on sampling parameters are separable (Feroz et al. 2009b) such that

$$\pi(\Theta_c) = \pi(x_c) \pi(y_c) \pi(c_{200}) \pi(M_{\text{tot}}(r_{200})) \pi(f_g(r_{200})) \pi(z). \quad (16)$$

We use Gaussian priors on cluster position parameters, centred on the pointing centre and with standard-deviation of 1 arcmin. We adopt uniform priors on c_{200} and a δ function prior on redshift z . The prior on $M_{\text{tot}}(r_{200})$ is taken to be uniform in $\log M$ in the range $M_{\text{min}} = 10^{14} M_\odot$ to $M_{\text{max}} = 6 \times 10^{15} M_\odot$ and the prior of $f_{\text{gas}}(r_{200})$ is set to be a Gaussian centred at the $f_{\text{gas}} = 0.12$ with a width of 0.02. A summary of the priors and their ranges are presented in Tab. 3.

In order to understand the underlying biases and constraints imposed by the priors and the model assumptions, we first study

Table 3. Summary of the priors on the sampling parameters. Note that $N(\mu, \sigma)$ represents a Gaussian probability distribution with mean μ and standard deviation of σ and $U(a, b)$ represents a uniform distribution between a and b .

Parameter	Prior
x_c, y_c	$N(0, 60)''$
c_{200}	$U(1, 10)$
$\log M_{\text{tot}}(r_{200})$	$U(14, 15.8) M_\odot$
$f_{\text{gas}}(r_{200})$	$N(0.12, 0.02)$

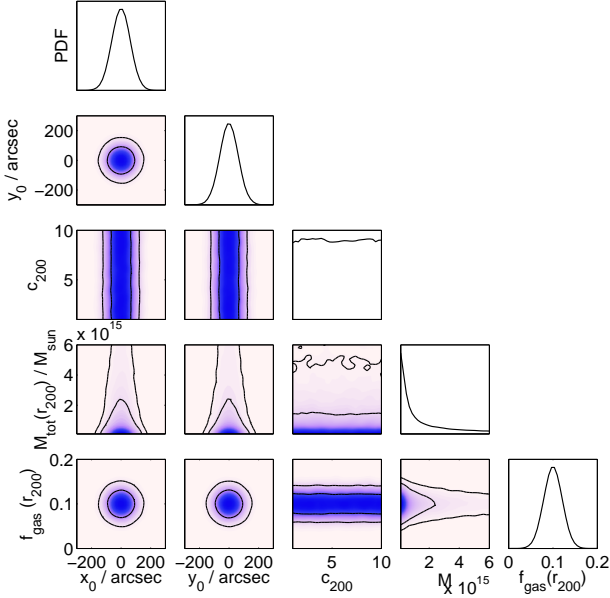


Figure 9. 1-D and 2-D marginalised posterior distributions of sampling parameters with no data.

our methodology in the absence of data. This can be carried out by setting the likelihood to a constant value and hence the algorithm just explores the prior space. Along with the analysis done using the simulated AMI data, this approach reveals the constraints that measurements of the SZ signal place on the cluster physical parameters and the robustness of the assumptions made. Fig. 9 represents 1-D and 2-D marginalised posterior distributions of a prior-only analysis for each of the sampling parameters in our model. The plots show that we correctly recover the assumed prior probability distributions of the sampling parameters in the absence of SZ data.

Fig. 10 shows 1-D and 2-D marginalised posterior distributions of sampling parameters for the first simulated SZ cluster data, with vertical lines representing the true parameter values and Fig. 11 shows the results of the analysis for A611. From the plots we notice that the model, along with its corresponding assumptions, can constrain cluster position and $M_{\text{tot}}(r_{200})$, but c_{200} remains relatively unconstrained. We also notice the weak negative degeneracy between $M_{\text{tot}}(r_{200})$ and c_{200} as we expect in high mass halos, between $1.0 \times 10^{14} M_\odot$ and $15.0 \times 10^{14} M_\odot$ (Pointecouteau et al. 2005; Salvador-Solé et al. 2007; Rudd, Zentner & Kravtsov 2008; Bhattacharya, Habib, & Heitmann 2011). From our analysis we find $M_{\text{tot}}(r_{200}) = (5.3 \pm 2.6) \times 10^{14} M_\odot$ and $r_{200} = (1.5 \pm 0.2) \text{ Mpc}$ for the simulated cluster and $M_{\text{tot}}(r_{200}) = (8.6 \pm 1.4) \times 10^{14} M_\odot$ and $r_{200} = (1.7 \pm 0.1) \text{ Mpc}$ for A611.

Figs. 12 and 13 present 1-D marginalised posterior distribu-

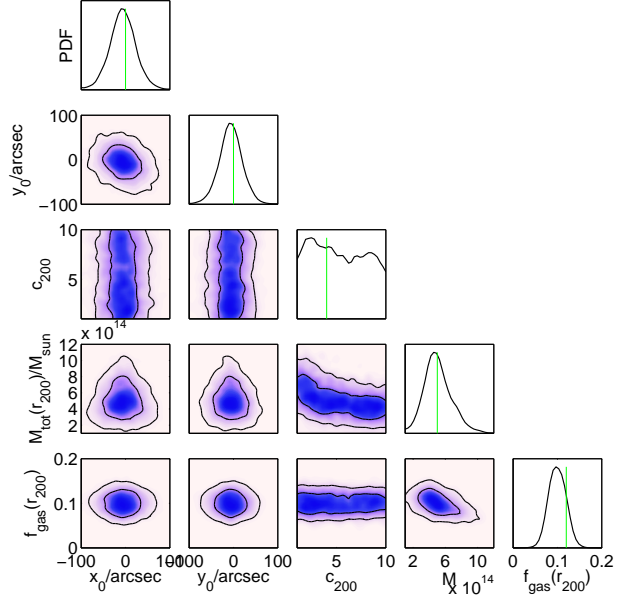


Figure 10. 1-D and 2-D marginalised posterior distributions of sampling parameters for the first simulated cluster.

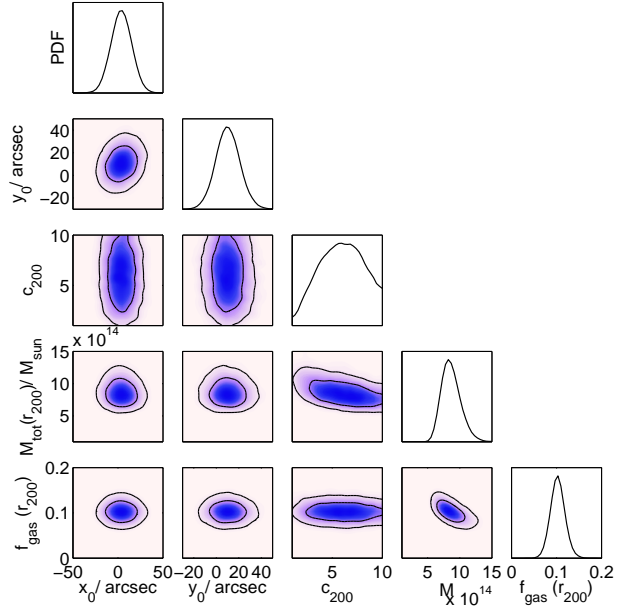


Figure 11. 1-D and 2-D marginalised posterior distributions of sampling parameters for A611.

tions of the model parameters (i.e. ρ_s , R_s , r_p and P_{ei}) for the first simulated cluster and A611 respectively. We note that although our data can constrain P_{ei} and r_p , ρ_s and R_s are not well constrained as they depend strongly on the relatively unconstrained cluster concentration parameter c_{200} . We use the best-fit values of these four parameters given in Tabs. 4 and 5 to determine the radial profiles of the clusters physical parameters according to our model.

As the SZ surface brightness is proportional to the line-of-sight integral of the electron pressure, (equations 12 and 13) SZ analysis of galaxy clusters provides a direct measurement of the pressure distribution of the ICM. Moreover, the integral of the Comptonization y parameter over the solid angle Ω subtended by

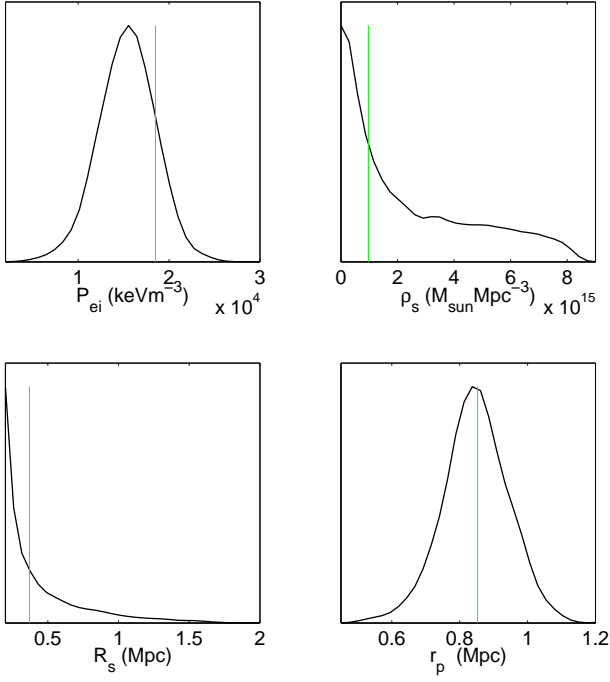


Figure 12. 1-D marginalised posterior distributions of the model parameters for the first simulated cluster. Green vertical lines are the derived values of the model parameters for a cluster defined by the input parameters given in the first row of Tab. 2

Table 4. Simulated cluster model parameters estimated (mean and standard deviation)

Parameter	μ	σ
$\rho_s (M_\odot \text{ Mpc}^{-3})$	2.52×10^{15}	2.31×10^{15}
$R_s (\text{kpc})$	402.79	306.83
$r_p (\text{kpc})$	846.93	95.88
$P_{ei} (\text{keV m}^{-3})$	1.54×10^4	3.08×10^3

the cluster (Y_{SZ}) is proportional to the volume integral of the gas pressure. It is thus a good estimate for the total thermal energy content of the cluster and its mass (see e.g. Bartlett & Silk 1994). Y_{SZ} parameter in both cylindrical and spherical geometries may be described as

$$Y_{\text{cyl}}(R) = \frac{\sigma_T}{m_e c^2} \int_{-\infty}^{+\infty} dl \int_0^R P_e(r) 2\pi s ds \quad (17)$$

$$Y_{\text{sph}}(r) = \frac{\sigma_T}{m_e c^2} \int_0^r P_e(r') 4\pi r'^2 dr' \quad (18)$$

where R is the projected radius of the cluster on the sky. In this con-

Table 5. Best-fit values of model parameters estimated (mean and standard deviation) for A611.

Parameter	μ	σ
$\rho_s (M_\odot \text{ Mpc}^{-3})$	2.87×10^{15}	2.07×10^{15}
$R_s (\text{kpc})$	361.80	209.31
$r_p (\text{kpc})$	1021.27	55.57
$P_{ei} (\text{keV m}^{-3})$	2.41×10^4	2.59×10^3

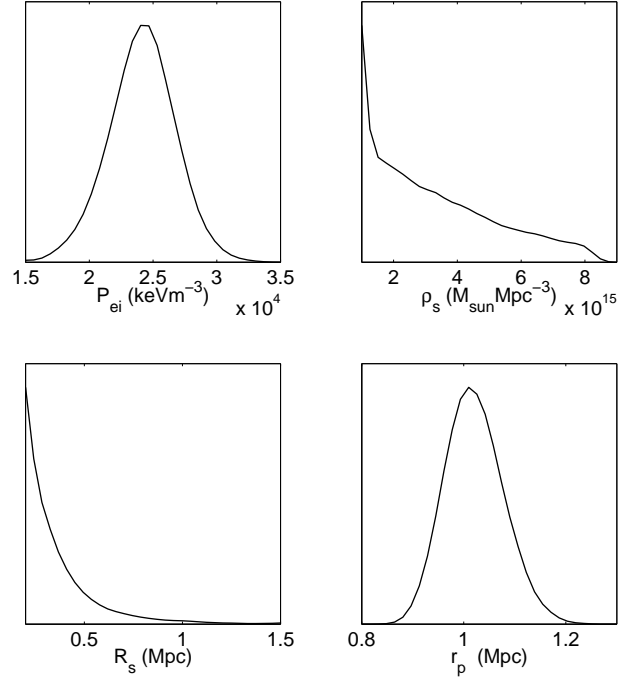


Figure 13. 1-D marginalised posterior distributions of the model parameters for A611.

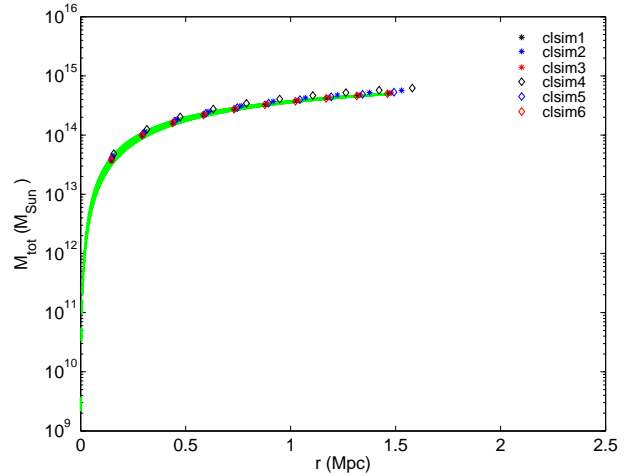


Figure 14. Profile of M_{tot} versus r for simulated clusters.

text we determined the radial profiles of M_{tot} and P_e as a function of r for six simulated clusters and A611 (figs. 14–17). In all figures, the background thick line shows the model prediction of the profiles of the clusters with the same mass as the clusters been analysed but vary in c_{200} as was illustrated in figs. 1–8. We have plotted the radial profiles of the corresponding cluster properties with coloured * and \diamond in case of simulated clusters and black * for A611. From the plots it is obvious that the radial trend of the clusters profiles are all consistent with our model prediction.

5 DISCUSSION AND CONCLUSIONS

We have studied the combination of NFW dark matter and GNFW gas pressure profiles within the hierarchical structure formation

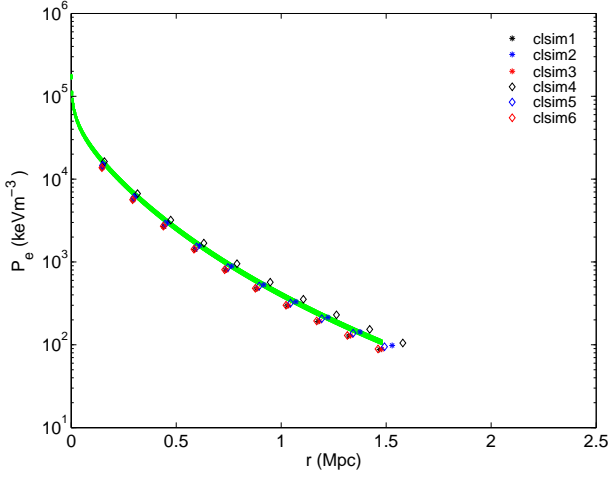


Figure 15. Profile of P_e versus r for simulated clusters.

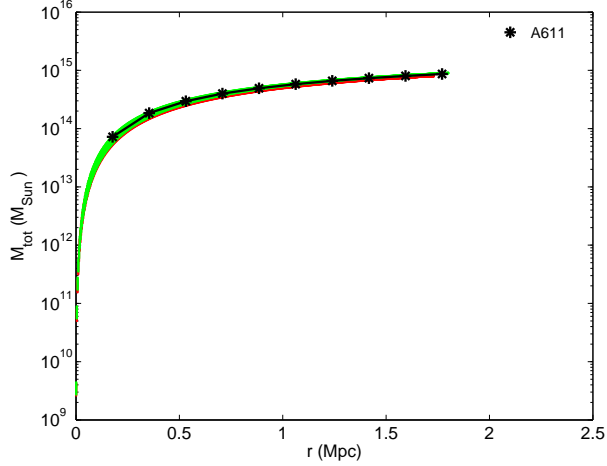


Figure 16. Profile of M_T versus r for A611.

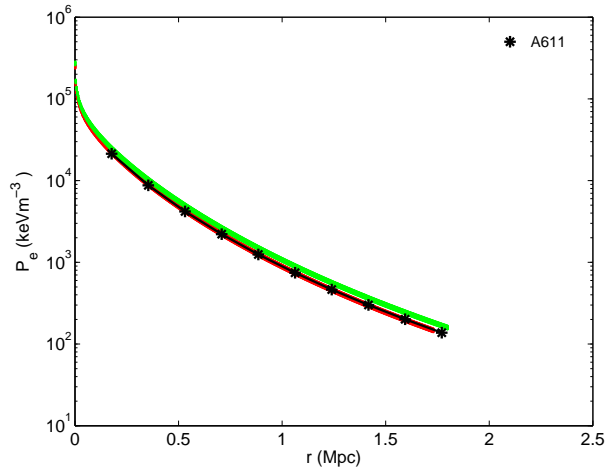


Figure 17. Profile of P_e versus r for A611.

scenario (Kaiser 1986) to derive the radial distribution of the cluster properties, assuming spherical symmetry, hydrostatic equilibrium, and that the local gas fraction throughout is small compared to unity.

Figs. 1 and 2 represent the dark matter density and enclosed mass profiles (the latter approximating the total enclosed mass profile under our assumption that $\frac{\rho_{\text{gas}}(r)}{\rho_{\text{tot}}(r)} \ll 1$ throughout). These results are based on the assumption of an NFW dark matter density profile, arising from the notion that the largest virialised structures form via gravitational collapse and merging. The profile has proved to be a good fit to the relaxed dark matter halos in high resolution N-body simulations down to 1% of the virial radius, and optical and X-ray observations of galaxy clusters both indicate that the profile is a good representation of the underlying cluster mass profile outside the core (Carlberg et al. 1997; Pratt & Arnaud 2002).

The electron pressure profiles are shown in Fig. 3, which are assumed to follow a GNFW profile. They exhibit self-similarity at the larger radii as they approach r_{200} and show dependency on the cluster mass. These behaviours are expected and resemble the profiles observed in a wide range of clusters (Holder et al. 2007; Nagai et al. 2007; Arnaud et al. 2010; Plagge et al. 2010; Mroczkowski et al. 2009) indicating that the pressure is least affected by non-gravitational phenomena in the ICM. This is important, in particular, in the analysis of Sunyaev-Zel'dovich observations of clusters, which essentially measure the line-of-sight integral of the ICM pressure through the cluster.

The derived gas density profiles $\rho_{\text{gas}}(r) = \mu_e n_e(r)$ are shown in Fig. 4, and reproduce all the main features observed both in numerical simulations and in real clusters (Sanderson et al. 2003; Borgani et al. 2004; Vikhlinin et al. 2005, 2006; Nagai et al. 2007; McCarthy et al. 2008). In particular, the profiles exhibit steepening at large radii, a power-law cusp at small radii (resulting from the fact that gas cooling and star formation processes have been taken into account in deriving the GNFW pressure profile) and a change of slope at intermediate radii. We also note that lower temperature clusters have lower gas density. The derived analytical expression for the gas density can thus model both the inner and outer regions of the clusters.

The derived electron/gas temperature profiles of the clusters are shown in Fig. 5. All of them have similar positive slopes up to $r \sim 0.1$ Mpc for the most massive clusters and have a broad peak around this region. The significant drop in the temperature in the innermost region is again because of taking into account the presence of radiative cooling mechanisms in deriving the GNFW pressure profile (Borgani et al. 2004; Vikhlinin et al. 2005, 2006; Pratt et al. 2007; Leccardi & Molendi 2008). In particular, we note that the clusters do not have isothermal cores. It should be pointed out, however, that real cluster data and current high-resolution simulations display complex temperature structures, which are the result of merging subgroups or supersonic accretion which heats the gas across the shock front where the assumption of hydrostatic equilibrium clearly breaks. Nonetheless, our derived temperature profile describes the general features of the ICM well, within our assumptions.

Fig. 6 shows the entropy profiles, which clearly show that the entropy depends on temperature and therefore the cluster mass. Moreover, the entropy profiles approach self-similarity as the radius approaches r_{200} , showing a scaling power-law distribution which is predicted in the models based on spherical gas accretion within a NFW dark matter halo (Tozzi & Norman 2001). This demonstrates that gravity dominates the ICM thermodynamics in the outer regions of clusters. These behaviours have already been

noted in the cluster numerical simulations (Kay et al. 2004; Borgani et al. 2004; Voit, Kay & Bryan 2005) and have also been observed in a large sample of galaxy clusters (Ponman, Sanderson and Finoguenov 2003; Piffaretti et al. 2005; McCarthy et al. 2008; Pratt et al. 2010). In the inner regions, on the other hand, the entropy profiles are clearly affected by the non-gravitational processes that have been considered in deriving the GNFw pressure profile.

Fig. 7 presents the enclosed gas mass profiles which increase with radius but with different slopes and fig. (8) shows the derived gas mass fraction profiles, which also exhibit a significant increase with radius, hence implying that f_{gas} can not be constant throughout the cluster as assumed by Mroczkowski (2011). Indeed, such an assumption is inconsistent with our other model assumptions as they lead to f_{gas} being a function of r . The profiles also show a pronounced dependency on the cluster mass, reflecting the dependency on the temperature as expected both from numerical simulations and X-ray observations of galaxy clusters using XMM and *Chandra* satellites (Ettori et al. 2004; Allen et al. 2004; Sadat et al. 2005; Vikhlinin et al. 2005, 2006; LaRoque et al. 2006; McCarthy et al. 2007; Afshordi et al. 2007).

Moreover, by numerically exploring the probability distributions of the cluster parameters given simulated interferometric SZ data in the context of Bayesian methods, and assuming our model with its corresponding assumptions, we investigate the capability of this model and analysis to return the simulated cluster input quantities. We find that simulated cluster physical parameters are well-constrained except c_{200} which is relatively unconstrained. We can also recover the true values of the simulated clusters. In particular, the mean cluster total mass estimate $M_{\text{tot}}(r_{200})$ and r_{200} for the first simulated cluster are: $M_{\text{tot}}(r_{200}) = (5.1 \pm 1.7) \times 10^{14} M_{\odot}$ and $r_{200} = (1.5 \pm 0.2) \text{ Mpc}$ and the corresponding true values of the simulated cluster are: $M_{\text{tot}}(r_{200}) = 5 \times 10^{14} M_{\odot}$ and $r_{200} = 1.5 \text{ Mpc}$. We determine the best-fit values of the parameters describing our model, i.e. ρ_s , R_s , R_p and P_{ei} , and hence calculate profiles of cluster total mass and gas pressure as determined using SZ data. We show that these profiles are consistent with our model.

We then repeat the analysis for a real cluster (A611) observed through its SZ effect with AMI. For this cluster, we find $M_{\text{tot}}(r_{200}) = (8.6 \pm 1.4) \times 10^{14} M_{\odot}$ and $r_{200} = (1.7 \pm 0.1) \text{ Mpc}$. A611 has previously been studied in different wave-bands. For example, Schmidt & Allen (2007) analysed *Chandra* data of A611 and found $M_{\text{tot}}(r_{200}) \approx 8 \times 10^{14} M_{\odot}$ and $r_{200} = 1.7 \text{ Mpc}$. Donnarumma et al. (2011) also studied *Chandra* X-ray data of A611 with different assumptions on background and metallicity. Their estimates of the cluster total mass vary from $M_{\text{tot}}(r_{200}) = (9.32 \pm 1.39) \times 10^{14} M_{\odot}$ for $r_{200} \approx 1.8 \text{ Mpc}$ to $M_{\text{tot}}(r_{200}) = (11.11 \pm 2.06) \times 10^{14} M_{\odot}$ for $r_{200} \approx 1.96 \text{ Mpc}$. They also carried out a strong lensing analysis of the cluster and found the mass estimates vary from $M_{\text{tot}}(r_{200}) = (4.68 \pm 0.31) \times 10^{14} M_{\odot}$ for $r_{200} \approx 1.4 \text{ Mpc}$ to $M_{\text{tot}}(r_{200}) = 6.32^{+0.51}_{-0.23} \times 10^{14} M_{\odot}$ for $r_{200} \approx 1.5 \text{ Mpc}$ when using different techniques. From weak lensing study of the cluster, Romano et al. (2010) find that the cluster total mass within radius of 1.5 Mpc is $(8 \pm 3) \times 10^{14} M_{\odot}$ from the aperture mass technique and $(5 \pm 1) \times 10^{14} M_{\odot}$ assuming parametric models. Our previous SZ analysis of A611 using isothermal β model (AMI Consortium: Shimwell et al. 2011) resulted in $M_{\text{tot}}(r_{200}) = (5.7 \pm 1.1) \times 10^{14} M_{\odot}$ and $r_{200} = (1.6 \pm 0.1) \text{ Mpc}$. Comparing the results of these studies with our analysis reveals that our results are in good agreement with the results of X-ray and weak lensing analyses of A611 but strong lensing and our previous SZ analyses of the cluster find a lower cluster mass which might be due to the extrapolating the strong lensing results in the outer spatial range as has been pointed out by Donnarumma et al. (2011)

and also the assumption of isothermality in our previous SZ study of the cluster.

We conclude that our proposed simple model for spherical galaxy clusters leads to realistic radial profiles for all the properties of interest, and hence may prove useful in the analysis of multi-wavelength cluster observations. An obvious future avenue for research, which we will explore in a follow-up paper to this letter, is to iterate the solution we have obtained by inserting the derived $\rho_{\text{gas}}(r)$ in (6) back into the expression for the total density $\rho_{\text{tot}}(r) = \rho_{\text{DM}}(r) + \rho_{\text{gas}}(r)$, recalculating the form of the other variables and repeating this process until convergence is established. In so doing, one might hope to obtain an even more realistic cluster model, but at the cost of losing a simple analytical formulation.

ACKNOWLEDGMENTS

The authors thank their colleagues in the AMI Consortium for numerous illuminating discussions regarding the modelling of galaxy clusters. The data analyses were carried out on the COSMOS UK National Supercomputer at DAMTP, University of Cambridge and we are grateful to Andrey Kaliazin for his computing assistance. MO acknowledges an STFC studentship.

REFERENCES

- Afshordi N., Lin Y.-T., Nagai D., Sanderson A. J. R., 2007, MNRAS, 378, 293
- Allen S. W., Schmidt R. W., Ebeling H., Fabian A. C., van Speybroeck L., 2004, MNRAS, 353, 457
- Allison J. R., Taylor A. C., Jones M. E., Rawlings S., Kay S. T., 2011, MNRAS, 410, 341
- AMI Consortium: Davies et al., 2011, MNRAS, 415, 2708
- AMI Consortium: Hurley-Walker N., et al., 2012, MNRAS, 419, 2921
- AMI Consortium: Olamaie M. et al., 2012, MNRAS, 419, 2921
- AMI Consortium: Rodriguez-Gonzalez C., et al., 2011, MNRAS, 414, 3751
- AMI Consortium: Shimwell T. et al., 2011, arXiv:1101.5590
- AMI Consortium: Shimwell et al., 2011, arXiv:1101.5590
- AMI Consortium: Zwart J. T. L., et al., 2008, MNRAS, 391, 1545
- AMI Consortium: Zwart J. T. L., et al., 2011, MNRAS, 418, 2754
- Arnaud M., Pratt G. W., Piffaretti R., Böhringer H., Croston J. H., Pointecouteau E., 2010, A&A, 517, A92
- Bartlett J. G., Silk J., 1994, ApJ, 423, 12
- Battaglia N., Bond J. R., Pfrommer C., Sievers J. L., Sijacki D., 2010, ApJ, 725, 91
- Battaglia N., Bond J. R., Pfrommer C., Sievers J. L., 2011, arXiv:1109.3709
- Battaglia N., Bond J. R., Pfrommer C., Sievers J. L., 2011, arXiv:1109.3711
- Bautz M. W., et al., 2009, PASJ, 61, 1117
- Bhattacharya S., Habib S., Heitmann K., 2011, arXiv:1112.5479
- Birkinshaw M., 1999, PhR, 310, 97
- Böhringer H., et al., 2007, A&A, 469, 363
- Borgani S., et al., 2004, MNRAS, 348, 1078
- Brunetti G., Cassano R., Dolag K., Setti G., 2009, A&A, 507, 661
- Carlberg R. G., et al., 1997, ApJ, 485, L13
- Carlstrom J. E., Holder G. P., Reese E. D., 2002, ARA &A, 40, 643
- Challinor A., Lasenby A., 1998, ApJ, 499, 1
- Donnarumma A., et al., 2011, A&A, 528, A73

- Ettori S., Tozzi P., Borgani S., Rosati P., 2004, *A&A*, 417, 13
- Feroz F., Hobson M. P., 2008, *MNRAS*, 384, 449
- Feroz F., Hobson M. P., Bridges M., 2009, *MNRAS*, 398, 1601
- Feroz F., Hobson M. P., Zwart J. T. L., Saunders R. D. E., Grainge K. J. B., 2009, *MNRAS*, 398, 2049
- Fixsen D. J., Cheng E. S., Gales J. M., Mather J. C., Shafer R. A., Wright E. L., 1996, *ApJ*, 473, 576
- George M. R., Fabian A. C., Sanders J. S., Young A. J., Russell H. R., 2009, *MNRAS*, 395, 657
- Grainge K., Jones M. E., Pooley G., Saunders R., Edge A., Grainger W. F., Kneissl R., 2002, *MNRAS*, 333, 318
- Hobson M. P., Maisinger K., 2002, *MNRAS*, 334, 569
- Holder G. P., McCarthy I. G., Babul A., 2007, *MNRAS*, 382, 1697
- Hoshino A., et al., 2010, *PASJ*, 62, 371
- Kaiser N., 1986, *MNRAS*, 222, 323
- Itoh N., Kohyama Y., Nozawa S., 1998, *ApJ*, 502, 7
- Kay S. T., Thomas P. A., Jenkins A., Pearce F. R., 2004, *MNRAS*, 355, 1091
- Kawaharada M., et al., 2010, *ApJ*, 714, 423
- Komatsu E., et al., 2011, *ApJS*, 192, 18
- LaRoque S. J., Bonamente M., Carlstrom J. E., Joy M. K., Nagai D., Reese E. D., Dawson K. S., 2006, *ApJ*, 652, 917
- Larson D., et al., 2011, *ApJS*, 192, 16
- Lau E. T., Kravtsov A. V., Nagai D., 2009, *ApJ*, 705, 1129
- Leccardi A., Molendi S., 2008, *A&A*, 486, 359
- Mason B. S., Myers S. T., 2000, *ApJ*, 540, 614
- McCarthy I. G., Babul A., Bower R. G., Balogh M. L., 2008, *MNRAS*, 386, 1309
- McCarthy I. G., Bower R. G., Balogh M. L., 2007, *MNRAS*, 377, 1457
- Mroczkowski T., et al., 2009, *ApJ*, 694, 1034
- Mroczkowski T., 2011, *ApJ*, 728, L35
- Nagai D., 2006, *ApJ*, 650, 538
- Nagai D., Kravtsov A. V., Vikhlinin A., 2007, *ApJ*, 668, 1
- Nagai D., Lau E. T., 2011, *ApJ*, 731, L10
- Nagai D., 2011, *MmSAI*, 82, 594
- Navarro J. F., Frenk C. S., White S. D. M., 1997, *ApJ*, 490, 493
- Nozawa S., Itoh N., Kohyama Y., 1998, *ApJ*, 508, 17
- Parrish I. J., McCourt M., Quataert E., Sharma P., 2012, *MNRAS*, 419, L29
- Piffaretti R., Jetzer P., Kaastra J. S., Tamura T., 2005, *A & A*, 433, 101
- Piffaretti R., Valdarnini R., 2008, *A&A*, 491, 71
- Plagge T., et al., 2010, *ApJ*, 716, 1118
- Planck Collaboration, et al., 2011, *A&A*, 536, A8
- Pointecouteau E., Giard M., Barret D., 1998, *A&A*, 336, 44
- Pointecouteau E., Arnaud M., Pratt G. W., 2005, *A&A*, 435, 1
- Ponman T. J., Sanderson A. J. R., Finoguenov A., 2003, *MNRAS*, 343, 331
- Pratt G. W., Arnaud M., 2002, *A & A*, 394, 375
- Pratt G. W., Böhringer H., Croston J. H., Arnaud M., Borgani S., Finoguenov A., Temple R. F., 2007, *A&A*, 461, 71
- Pratt G. W., et al., 2010, *A&A*, 511, A85
- Rephaeli Y., 1995, *ARA & A*, 33, 541
- Reiprich T. H., et al., 2009, *A&A*, 501, 899
- Romano A., et al., 2010, *A&A*, 514, A88
- Rudd D. H., Zentner A. R., Kravtsov A. V., 2008, *ApJ*, 672, 19
- Salvador-Solé E., Manrique A., González-Casado G., Hansen S. H., 2007, *ApJ*, 666, 181
- Sadat R., et al., 2005, *A&A*, 437, 31
- Sanderson A. J. R., Ponman T. J., 2003, *MNRAS*, 345, 1241
- Schmidt R. W., Allen S. W., 2007, *MNRAS*, 379, 209
- Simionescu A., et al., 2011, *Sci*, 331, 1576
- Sunyaev R. A., Zeldovich Y. B., 1970, *CoASP*, 2, 66
- Tozzi P., Norman C., 2001, *ApJ*, 546, 63
- Urban O., Werner N., Simionescu A., Allen S. W., Böhringer H., 2011, *MNRAS*, 414, 2101
- Venturi T., Giacintucci S., Dallacasa D., Cassano R., Brunetti G., Bardelli S., Setti G., 2008, *A&A*, 484, 327
- Vikhlinin A., Kravtsov A., Forman W., Jones C., Markevitch M., Murray S. S., Van Speybroeck L., 2006, *ApJ*, 640, 691
- Vikhlinin A., Markevitch M., Murray S. S., Jones C., Forman W., Van Speybroeck L., 2005, *ApJ*, 628, 655
- Voit G. M., 2005, *RvMP*, 77, 207
- Voit G. M., Kay S. T., Bryan G. L., 2005, *MNRAS*, 364, 909